ORIGINAL RESEARCH ARTICLE

The Depositional Record
A journal of the International Association of Sedimentologists

WILEY

Testing geological proxies for deep-time tidal model simulations

B. Guo[1,2] | L. A. M. Fitzgerald[1] | J. M. Hewitt[1] | O. Pampaloni[1] |
J. A. M. Green[1]

[1]School of Ocean Science, Bangor
University, Menai Bridge, UK

[2]Engineering School, Cardiff University,
Cardiff, UK

Correspondence
J. A. M. Green, School of Ocean
Science, Bangor University, Menai
Bridge, UK.
Email: m.green@bangor.ac.uk

Abstract

Tides are a key driver of a range of Earth system processes, and we now have the capacity to simulate tidal dynamics on a range of temporal and spatial scales. Deep-time tidal model simulations have been used to provide insight into past ocean circulation patterns, evolution of life and the developments of the Earth-Moon system's orbital configuration. However, these tidal model simulations are relatively poorly constrained and validated because of a lack of readily available proxies. The feasibility of using two types of proxy is explored here; (1) sedimentary deposits which can directly estimate palaeotidal ranges, and (2) black shale, to constrain three palaeotidal model simulations for different time slices. Specifically, three palaeotidal range proxies were used for the early Devonian (400 Ma), three palaeotidal range proxies and five black shales for the lower Jurassic (185 Ma), and eight black shales for the early Cretaceous (95 Ma). Both tidal proxies confirm the tidal model results in most locations. The model results for 400 Ma and 185 Ma matched 2/3 of the palaeotidal range proxies for each of these periods. The locations of black shale were compared with tidal front locations predicted by the model outputs based on the Simpson–Hunter parameter and the model results from 95 to 185 Ma agree with the black shale proxies in 10/13 of the locations. In the cases where there is a disagreement, the model resolution is probably too low to fully resolve the details of the coastal topography, or—in one case—the palaeobathymetry is incorrect. Consequently, it is argued that it is worth expanding this type of work, and that such data can be used to validate both models and reconstructions.

KEYWORDS

black shale, palaeotidal modelling, palaeotidal range, tidal proxy, tidalites, tides

1 | INTRODUCTION

Ocean tides impact a range of Earth system processes. They control the locations of productive shelf sea fronts (Simpson & Hunter, 1974), sustain the climate-regulating global overturning circulation (Wilmes et al., 2021; Wunsch & Ferrari, 2004), drive ocean primary production (Sharples et al., 2007; Tuerena et al., 2019) and set the environment for key evolutionary events (Balbus, 2014; Byrne et al., 2020). The dissipation of tidal energy also slows down Earth's spin and forces the moon to recede to conserve angular momentum (Bills & Ray, 1999; Daher et al., 2021), meaning the tides are a first-order controller of daylength. Recent tidal model results (Green et al., 2017, 2018) show significantly less energetic tides in the past. This has far-reaching consequences for the Earth system, for example, its biogeochemical cycles, and may have been a driving force in the oxygenation of the atmosphere (Klatt et al., 2021).

Numerical modelling of palaeotides relies on tectonic reconstructions for boundary conditions (see Green et al., 2022, and references above). However, despite numerous publications outlining characteristics of palaeotides from the palaeobiological and geological records, numerical simulations are poorly constrained as the proxy information is not readily accessible to the modelling community. This is partially rectified by collating information on deep-time tides from different sources and using these data to constrain numerical tidal model simulations for three time slices: 400, 185 and 95 Ma. These were chosen for their representative nature and the availability of suitable proxy data in the literature. The results can also benefit the regional palaeogeographical reconstructions: if the tidal conditions are verified at a location, the regional topography is accurate as well.

Palaeotidal range estimates were obtained from results presented in the literature; palaeotidal range is determined through palaeoenvironmental interpretation, and may be estimated by analogy to modern tidal environments (Klein, 1971; Wells et al., 2005). For instance, small-scale sedimentary structures are usually distributed in mesotidal environments (Reineck, 1975), while large-scale structures or plane beds are in macrotidal settings (Dalrymple et al., 1990). However, these interpretations may only provide a rough estimate of the tidal range, rather than an accurate definition (Collins et al., 2021). Furthermore, well-preserved tidalites display ebb-flood, and spring-neap or spring-neap-like cycles, alongside signals of the diurnal inequality, and can be used to constrain days per month and days per year counts in the geological past (Archer, 1996; Coughenour et al., 2009). Under ideal conditions, tidal range in a specific location can be directly estimated from tidalites

where complete, fining-upward sequences of sediment are preserved (Devries Klein, 1971; Slingerland, 1986; Tanavsuu-Milkeviciene & Plink-Bjorklund, 2009; Williams, 2000). For example, the sharp contrast of thin neap couplets and thick spring couplets in tidal bundles suggested macrotidal range or higher (Tessier & Gigot, 1989). In other cases, the palaeotidal range could be estimated from the stratigraphic thickness of intertidal deposits in tidal flat units (Klein, 1970, 1971). Sediment can sometimes also be translated into a tidal current range based on bedload transport rates for non-cohesive sediments (Ward et al., 2020), where fine-grained sediments (silt and clay) are more common at low tidal ranges. However, exploring this aspect falls outside the scope of this study.

Furthermore, tidal mixing fronts separate a vertically mixed water column from a stratified one (Bowers & Simpson, 1987; Simpson & Bowers, 1981; Simpson & Hunter, 1974). Their positions are determined by the tidal current magnitude and the water depth, and they are found near contours of

$$\chi = H / u^3 = 200 \qquad (1)$$

where H is water depth (m), and u is the tidal current magnitude (m^2/s); χ the commonly referred to as the Simpson–Hunter parameter (m^2/s^3). Consequently, mapping the fronts provides a proxy for palaeotidal current magnitudes. Black shale deposition occurs in poorly ventilated anoxic conditions incompatible with strong tidal currents (Abdi et al., 2021; He et al., 2022; Stow et al., 2001; Wignall & Newton, 2001). It is expected therefore that the presence of a black shale in the geological record will indicate a strongly stratified water column, which can be tracked through the locations of the tidal mixing fronts (Simpson & Hunter, 1974). Note that the specific driver leading to the anoxic event is not important, rather the fact that a well-mixed water column is also well-ventilated and if the water column is mixed, all properties are mixed too. The tides provide a continuous supply of mechanical energy for mixing and a black shale must therefore sit in a stratified regime. A similar method, tracking microfossil assemblages, has also been suggested but will not be pursued here (Scourse et al., 2002).

To date, a few proof-of-concept studies used tidal deposits to constrain numerical tidal model simulations (Byrne et al., 2020; Green et al., 2020; Wells et al., 2010; Zuchuat et al., 2022), but the information used was limited to a few data points for specific regions and time slices. Consequently, this paper presents a systematic comparison between environmental proxies and numerical tidal model results.

TABLE 1 Forcing parameters used in the model simulations, with data from Daher et al. (2021). The M$_2$ forcing factor is based on the change in lunar distance associated with the change in orbital periods. The K$_1$ forcing factor is made up of 2/3 from the Moon and 1/3 from the Sun.

Time slice (Ma)	Sidereal day	M$_2$ period (h)	S$_2$ period (h)	K$_1$ period (h)	M$_2$ forcing factor	K$_1$ forcing factor
400	21.95	11.01	10.58	21.95	1.11	1.07
185	23.19	11.77	11.35	23.19	1.05	1.03
95	23.49	12.18	11.78	23.49	1.01	1.01
PD	23.93	12.42	12.00	23.93	1.00	1.00

2 | TIDAL MODELLING

The simulations of past tides were made using OTIS—the Oregon State University Tidal Inversion Software—a dedicated tidal model which has been used extensively to simulate deep-time and present day (PD) tides (Blackledge et al., 2020; Byrne et al., 2020; Egbert et al., 2004; Green et al., 2022). OTIS was benchmarked against other forward tidal models and was shown to perform well (Stammer et al., 2014) which provides a numerical solution to the linearised shallow-water equations forced by the tide only, as presented by the following Equations (2) and (3):

$$\frac{\partial \mathbf{U}}{\partial t} + f \times \mathbf{U} = gH\nabla\left(\eta - \eta_{\mathrm{SAL}} - \eta_{\mathrm{EQ}}\right) - \mathbf{F} \quad (2)$$

$$\frac{\partial \eta}{\partial t} - \nabla \times \mathbf{U} = 0 \quad (3)$$

Here, $U = u\,H$ is the tidal volume transport (u is the horizontal velocity vector [m/s] and H is the water depth [m]), f the Coriolis parameter (rad/s), g the acceleration due to gravity (m/s^2), η the sea-surface elevation (m), η_{SAL} the self-attraction and loading elevation (m), η_{EQ} is the elevation of the equilibrium tide (m) and F the tidal energy dissipation term (W/kg or m^2/s^3). The dissipation is parameterised through two components, denoted F_{B} and F_{W} respectively, representing bed friction and energy losses due to tidal conversion, that is, the energy transferred into a baroclinic tide respectively. Friction is parameterised using the standard quadratic law, $F_{\mathrm{B}} = C_{\mathrm{D}}u|u|$, where $C_{\mathrm{D}} = 0.003$ is a dimensionless drag coefficient (Taylor, 1920), whereas the tidal conversion term may be written as $F_{\mathrm{W}} = C\,U$, with a conversion coefficient, C, expressed by following Equation 4 (Green & Nycander, 2013; Zaron & Egbert, 2006):

$$C(x,y) = \gamma \frac{N_{\mathrm{H}}\overline{N}}{8\pi\omega}(\nabla H)^2 \quad (4)$$

Here, $\gamma = 50$ represents a dimensionless scaling factor representing unresolved bathymetric roughness, N_{H} is the buoyancy frequency at the seabed (unit of s^{-1}), $\overline{N}$ represents the vertical average of the buoyancy frequency (rad/s) and ω the frequency of the tide. The buoyancy frequency, N (rad/s), is given by $N^2 = -g/\rho\partial\rho/\partial z$, where ρ is the density (kg/m^3). The details of the density field are not known for the period discussed here, so the values of N based on a statistical fit to observed PD values presented by Zaron and Egbert (2006) were used. Consequently, $N(x,y) = 0.00524\exp(-z/1300)$, where z is the vertical coordinate (m), and the constants 0.00524 and 1300 have units of s^{-1} and m respectively. The model results are relatively insensitive to changes in stratification and this parameter space is not explored further (Byrne et al., 2020; Egbert et al., 2004; Green et al., 2020).

2.1 | Reconstructions and simulations

The palaeobathymetry data came from Scotese and Wright (2018) and were supplied at 1/10° horizontal resolution in both latitude and longitude. All bathymetries effectively ran from 89° S to 89° N in latitude due to the introduction of land at the poles to handle the convergence of the model grid cells at high latitudes. Note that outside of near-resonant states, tidal simulations are relatively insensitive to small-scale topographic changes and the blocking of the poles (Egbert et al., 2004; Wilmes & Green, 2014). The details for each era are summarised below and described in more detail in each section.

All time slices were simulated for the M$_2$, S$_2$ and K$_1$ constituents. All time slices were simulated using PD tidal forcing as well as changed forcing to parameters relevant for each time slice (Daher et al., 2021)—see Table 1 for details. The model outputs the amplitudes and phases of the surface elevations, η, and transports, U, for each of the constituents.

3 | PROXIES

Two types of tidal proxies are explored here: (1) sedimentary deposits that can be used to directly estimate

palaeotidal range and (2) black shale (BS), which indirectly estimate tidal conditions.

3.1 | Direct proxies: Palaeotidal range

Here, palaeotidal ranges interpreted from tidal deposits in the literature are regarded as 'direct proxies' (DPs); these have been used previously to constrain palaeotidal modelling (Byrne et al., 2020; Green et al., 2020; Zuchuat et al., 2022). Tidal ranges from the literature were categorised into the four standard categories: microtidal (0–2 m), mesotidal (2–4 m), macrotidal (4–6 m) and hypertidal (>6 m; Archer, 2013; note that the oceanographic literature use megatidal for a range >6 m). In this investigation,

if the results from the tidal model for a proxy location fall within the category provided by the proxy, the simulation is considered accurate. Palaeotidal range proxies will be used to validate the simulations for 400 Ma and 185 Ma. Details of the direct tidal proxies are summarised below and in Tables S1A and S1B in the Supplementary Information and the locations are presented in Figure 1A,B.

Three palaeotidal range proxies for 400 Ma were found in the literature, all also used by Byrne et al. (2020); note that the simulations here use a different reconstruction and higher resolution than Byrne et al. (2020) did. A meso–macrotidal regime was discovered in the fine to coarse-grained, tide-dominated deltaic deposits of the Rezekne and Pärnu formations in the Devonian Baltic Basin; these make up (Direct proxy 1) DP1 (Figure 1A; Tanavsuu-Milkeviciene & Plink-Bjorklund, 2009; Tovmasjana, 2013). Another meso–macrotidal environment was found in the rippled and cross-bedded siliciclastic and dolomitic tidal flat facies of the Padeha Formation in the Tabas Block of the Central-East Iranian Microcontinent (DP2; Wendt et al., 2004; Zand-Moghadam et al., 2014). Griffing et al. (2000) and Rust et al. (1989) inferred a mesotidal regime from the tidally deposited sandstone and mudstone bodies in the Cap-aux-Os Member of the Battery Point Formation in the Catskill Clatic Wedge, Canada (DP3 in Figure 1A).
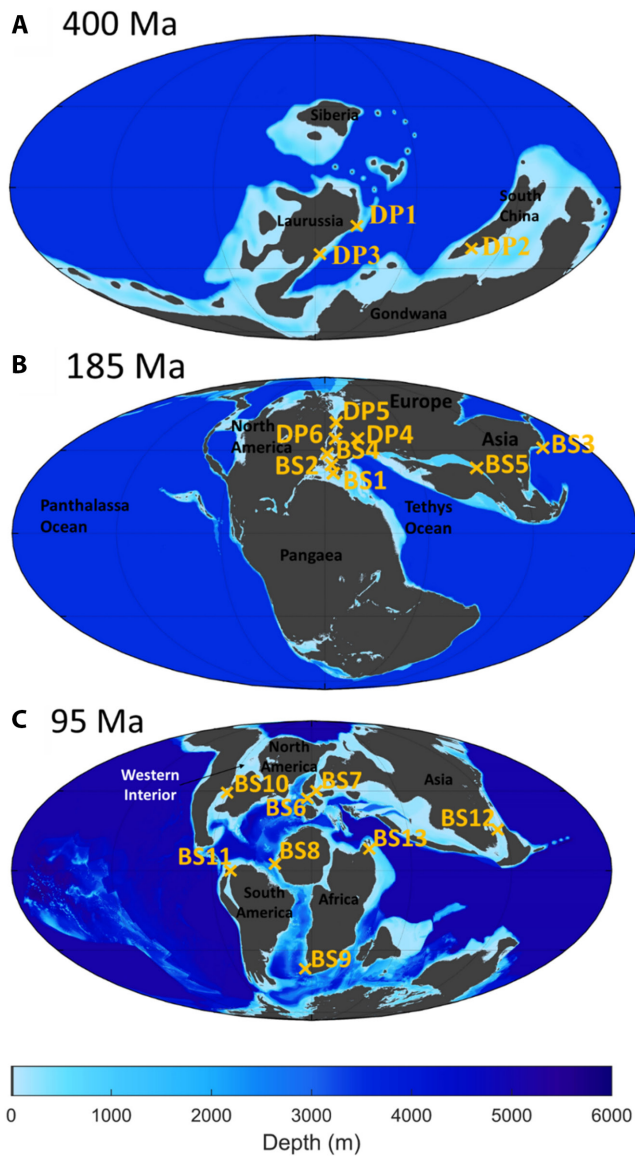

FIGURE 1 The palaeogeographical reconstructions and the location of tidal proxies for (A) 400 Ma; (B) 185 Ma; (C) 95 Ma, with the specifics of direct proxies (DP) and black shales (BS).
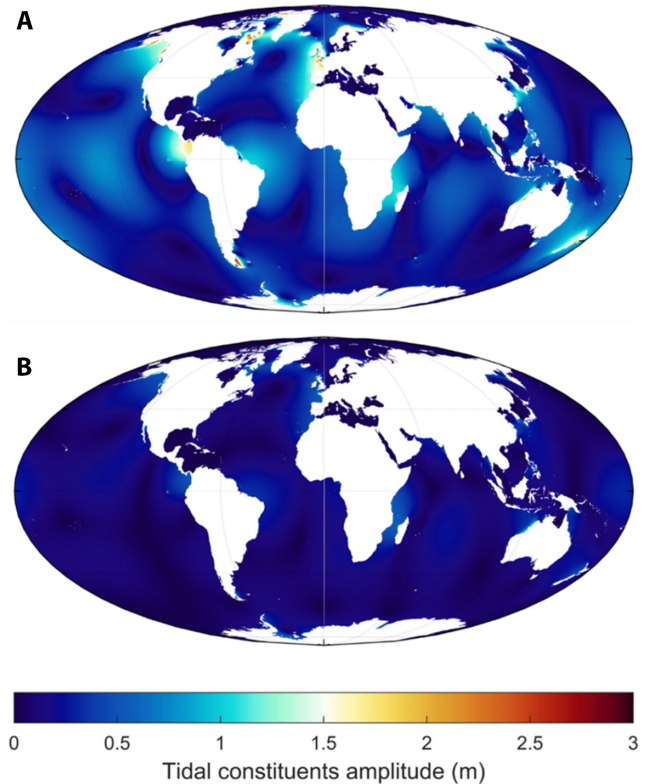

FIGURE 2 (A) The simulated M_2 tidal amplitudes in metres for the PD control simulations; (B) The simulated S_2 tidal amplitudes.
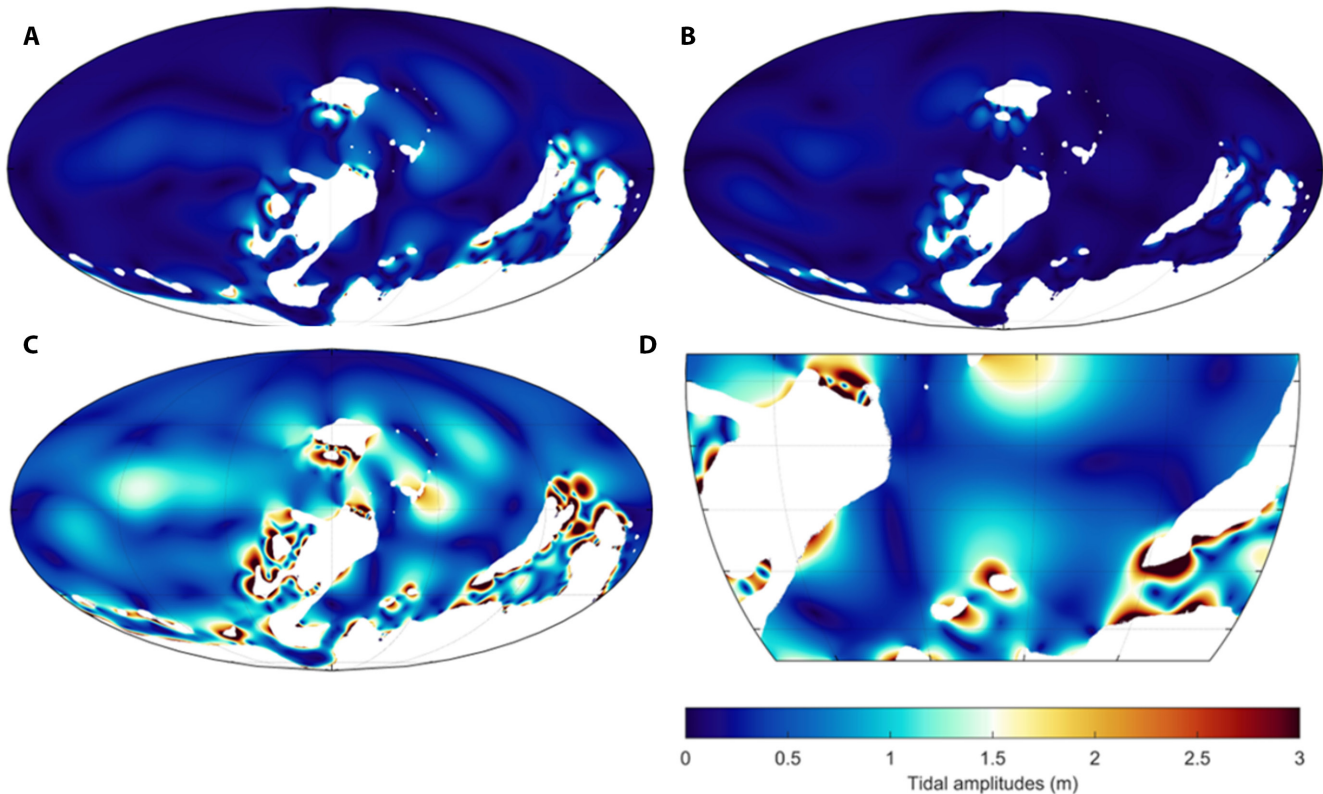
FIGURE 3 (A) Simulated M_2 tidal amplitudes; (B) simulated S2 tidal amplitudes; (C) simulated mean spring tidal range for 400 Ma, calculated by $2(\eta_{M_2} + \eta_{S_2})$, and the marked palaeotidal range proxies; (D) close-up of ocean region surrounding Laurussia.
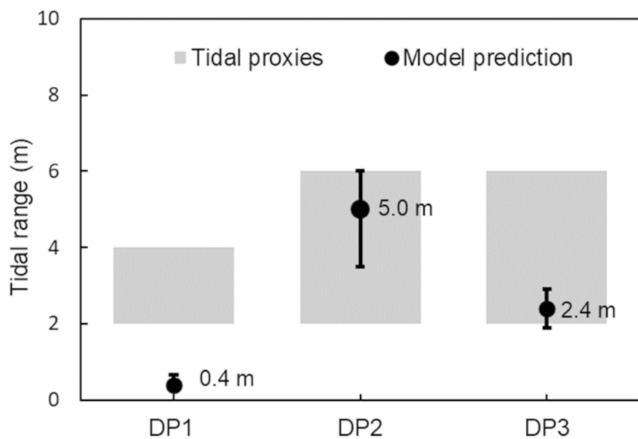

FIGURE 4 The tidal range indicated by direct proxies and the corresponding model prediction for 400 Ma. The modelled tidal range is the range in the gridcell nearest to the proxy location, where the error bar shows the largest and smallest values in a 3×3 grid box centred on the proxy location.

For the 185 Ma time slice, three direct proxies were found in the literature (Figure 1B). Sellwood (1972) determined the minimum tidal range as 1 m from the thickness of sandstone channel-fill sequences in Gry's Lower Coal Series in Bornhom, Denmark (DP4). A macrotidal regime was concluded based on the dimensions of estuarine bedforms in the incised valleys of the Ostreaelv Formation (DP5) in the Niell Klinter Group in Jameson Land, Greenland (Ahokas et al., 2014). Lastly, the Helsingborg Member of the Gassum Formation in southern Sweden and the Galgeløkke Member of the Rønne Formation on Bornholm (both combined as DP6) consisting of tidal flat and channel facies, were deposited in a microtidal to mesotidal environment (Nielsen et al., 1989).

3.2 | Indirect proxies: Black shale

It has been suggested that tidal rhythmites, which can indicate palaeotidal range, are predominantly formed within middle to inner estuaries (Tessier, 2023). This can introduce uncertainties when validating tidal model results because the reconstruction is unlikely to cover small-scale estuaries. Furthermore, where direct proxies have been found for the tidal regimes, these are almost all meso–macrotidal, leaving low tidal ranges without proxies (at this stage). To address this, it is proposed that locations of black shale constitute an additional tidal proxy for tides in a shelf sea setting.

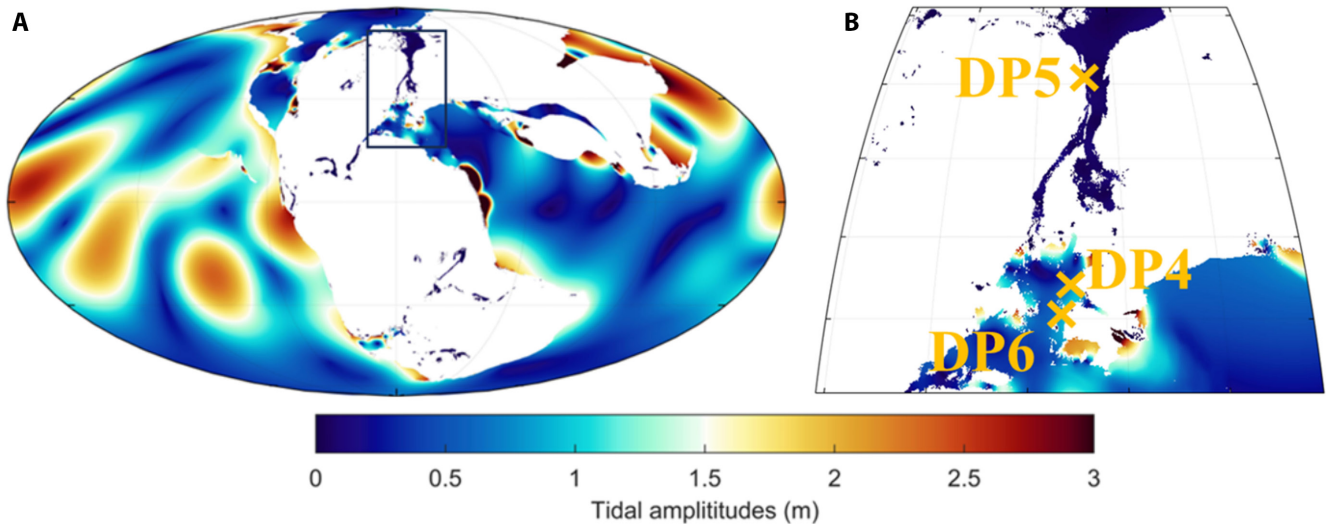Black shale is an indirect proxy which can ultimately constrain tidal current velocities. Tide-driven mixing

FIGURE 5 (A) Simulated mean spring tidal amplitudes for the 185 Ma time slice; (B) close-up of the Laurasian Seaway where the proxies are located.
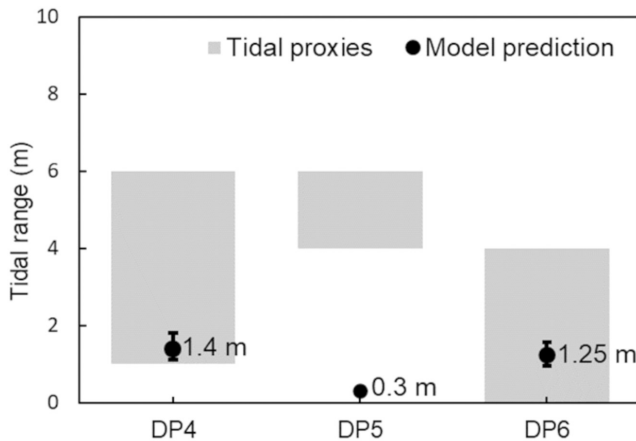

FIGURE 6 The M_2 tidal range indicated by direct proxies and the corresponding model prediction for 185 Ma. Note that in this figure, DP4 has been moved from the original location on land to the nearest coastal ocean grid cell.

controls stratification in shelf seas, with a tidal mixing front marking the point between vertically mixed and stratified areas as discussed in the introduction. Mapping front positions from the model output and comparing them to locations with black shale therefore constitutes a validation metric: the shale must sit on the stratified side of the front and if they do not, the model simulation is probably incorrect. The identified palaeo-locations of the black shale formations used here are shown as 'BS' in Figure 1B,C. A total of 13 locations were identified: five for the 185 Ma timeslice and a further eight for 95 Ma. Note that black shale deposits in deep water will not be considered here, as anoxia in the deep ocean is not controlled by tides. Furthermore, black shale deposited between the Precambrian (400 Ga) to the Devonian (419–358 Ma) was

deposited at a time when ocean chemistry was significantly different and there is evidence to suggest that there was not enough oxygen in the marine environment to form oxic waters (Aharon, 2005; Kimura & Watanabe, 2001).

4 | RESULTS

4.1 | PD model validation

The performance of the PD set-up of the tidal model was evaluated compared to the TPXO9 satellite altimetry constrained product (Egbert & Erofeeva, 2002). The predicted M_2 and S_2 tidal amplitudes for PD are presented in Figure 2, with the globally spatial-averaged root-mean-square (RMS) errors for M_2 and S_2 amplitudes calculated to be 9.8 cm and 4.4 cm respectively.

4.2 | 400 Ma

The predicted M_2 and S_2 amplitudes and the mean spring tidal range at 400 Ma are presented in Figure 3A,B. A region with high amplitudes of M_2 and S_2 is situated in the western and northern parts of Laurussia, southern Siberia and the north-east of Gondwana, where the M_2 amplitude exceeds 1.5 m, while S_2 amplitude exceeds 1 m. Less energetic waters are found in east Laurussia and northern Siberia as M_2 or S_2 microtidal regimes dominate these areas. The model prediction here is generally consistent with the lower-resolution simulations for 400 Ma from Byrne et al. (2020), but variations in tidal predictions occur in specific areas due to differences in the utilised palaeobathymetry data. For instance, this study reveals

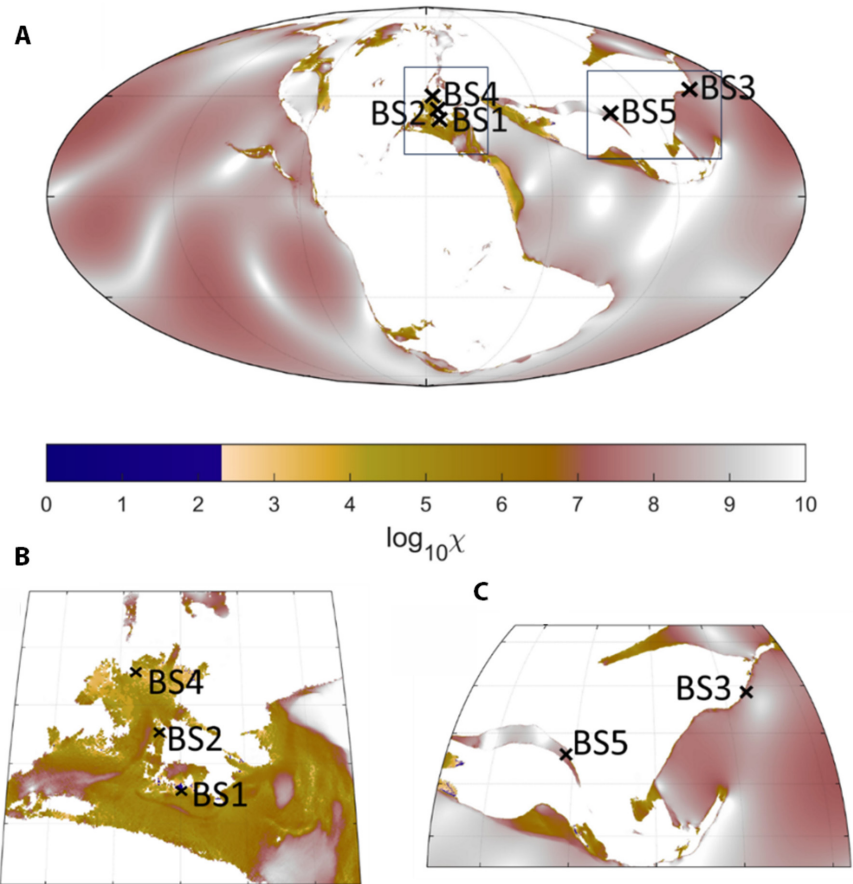FIGURE 7 Predicted Simpson–Hunter criterion for 185 Ma, and the palaeo-location of black shale proxies.

TABLE 2 The model prediction of Simpson–Hunter criterion (χ) and associated stratification state for the 185 Ma time slice.

	BS1	BS2	BS3	BS4	BS5
$\log_{10}\chi$	2.0	3.8	7.9	4.1	8.0
Water column structure	Mixed	Stratified	Stratified	Stratified	Stratified

significantly higher M_2 amplitudes in southern Siberia (up to 2.5 m) and lower S_2 amplitudes in north-east Laurussia (lower than 0.5 m) compared to the prediction from Byrne et al. (2020).

The mean spring tide range is computed as $2\left(\eta_{M_2} + \eta_{S_2}\right)$, as shown in Figure 3C,D, where η_{M_2} and η_{S_2} are the corresponding tidal amplitudes for principal lunar semidiurnal (M_2) and principal solar semidiurnal (S_2). Macrotidal areas (4–6 m) are located along the west and north coastline of Laurussia, southern Siberia and north-east region of Gondwana. In contrast, mesotidal regions (2–4 m range) were found on the south-east coast of Laurussia. Compared with direct tidal proxies collected for 400 Ma and plotted in Figure 4, the model prediction matches reasonably well with the proxies at DP3 and DP2 (see Table S1A for details). However, the simulation does not agree with the tidal proxy of the DP1. DP1 was located in a meso–macrotidal delta, whereas the simulation indicates a microtidal environment in that region. This discrepancy may be an effect of model resolution: the Pärnu

and Rēzekne formations were deposited in transitional fluvial-tide-dominated flats, tidal channels or in a deltaic distributary channel that, at the current model resolution, is not resolved.

4.3 | 185 Ma

The 185 Ma model results are validated using both tidal range proxies and black shale (see Table S1B for a summary of proxy information). It should be noted that DP4 (Gry's Lower Coal Series) will not work as a tidal proxy because it is too far inland. This is of course still useful information because it tells us that the reconstruction needs to be modified to encompass the proxy location. These simulations host a relatively weak global tide, except for a macrotidal regime in the western Tethys Sea (Figure 5). It can be argued that if DP4 is moved to the nearest coastal grid cell, it fits well with the tidal model result of 1.4 m M_2 tidal range (Figure 6). The predicted

tidal range at DP6 (Helsingborg Member of the Gassum Formation and the Galgeløkke Member of the Rønne Formation) is 1.25 m, which is in the range of the tidal proxy there (Figure 6). However, the tidal range prediction at the DP5 site (Ostreaelv Formation) is 0.30 m, which is a considerable underestimate compared to the 4–6 m macrotidal range was identified in the proxy. It is proposed that this is another resolution issue with the model grid: a macrotidal range in a shallow seaway may not be fully resolved with a 1/10° model resolution, resulting in the omission of a resonant feature in the inner part of the seaway.

The calculated Simpson–Hunter criterion for 185 Ma in Figure 7 and Table 2 shows that the model result matches four of five black shale tidal proxies (BS2–BS5). BS1 is located at a borderline mixed region with a value of $\log_{10}\chi \sim 2$ in the model simulations, whereas the proxy of course points to a stratified water column. This could be remedied by increasing the depth of the area to reduce current speeds and increase χ, as demonstrated by Equation (1). Again, the tidal proxies give information about the quality of the tectonic reconstructions as well as acting as a validation tool for the tides.

4.4 | 95 Ma

The predicted M_2 amplitude and its corresponding velocity magnitude for the 95 Ma time slice are presented in Figure 8. In general, this is a quiescent time slice, with weak tides in the vast epeiric seas covering PD Africa, Asia and Europe. The exceptions are high-velocity zones northeast of PD Madagascar and north Australia (Figure 8A).

There is a lack of direct tidal proxies for 95 Ma and instead the Simpson–Hunter criterion and black shale formations will be used as proxies. The results shown in Figure 9 indicate that much of the 95 Ma shelf seas were stratified and that the black shale records are matched by the modelled stratification in six of eight locations (see Table 3). The two mismatched locations, BS10 and BS12, are again located at the boundary of mixed and stratified regions with values of $\log_{10}\chi = 2.0$ and 1.8 respectively. A small correction of the depth would also ensure a stratified water column at these two locations. The positive correlation between black shale palaeo-locations and tidal front locations suggests that black shale can serve as indirect proxies for palaeotides.

5 | DISCUSSION

Simulations of the tides for three deep-time time slices are presented with the results validated with two types of geological tidal proxies: palaeotidal ranges deducted from tidal deposits (a direct proxy) and black shale (an indirect proxy). Direct proxies were collected from published literature for 400 and 185 Ma; for both time slices, the model performed reasonably well with proxies agreeing in 2/3 of the locations. However, in areas where it fell short, it is argued that the bathymetry of the reconstruction could be modified to ensure a better fit. Using direct proxies is the preferred method for validating palaeotidal models (Byrne et al., 2020; Zuchuat et al., 2022) but they are rare in the literature. Therefore, it is proposed to use black shale as an indirect proxy, providing an upper limit of the tidal current speeds, with a proof-of-concept study presented for time slices at 185 and 95 Ma. Because of the interconnections between tidal current speeds, stratification and potential for anoxia, it is argued that in cases where the Simpson–Hunter parameter denotes a stratified water column (i.e. $\log_{10}\chi > 2$–2.3), the presence of black shale in that region can be attributed to the water-mass stratification. The results and proxies agree in 10 of 13 locations across both time slices. It would be easy to change
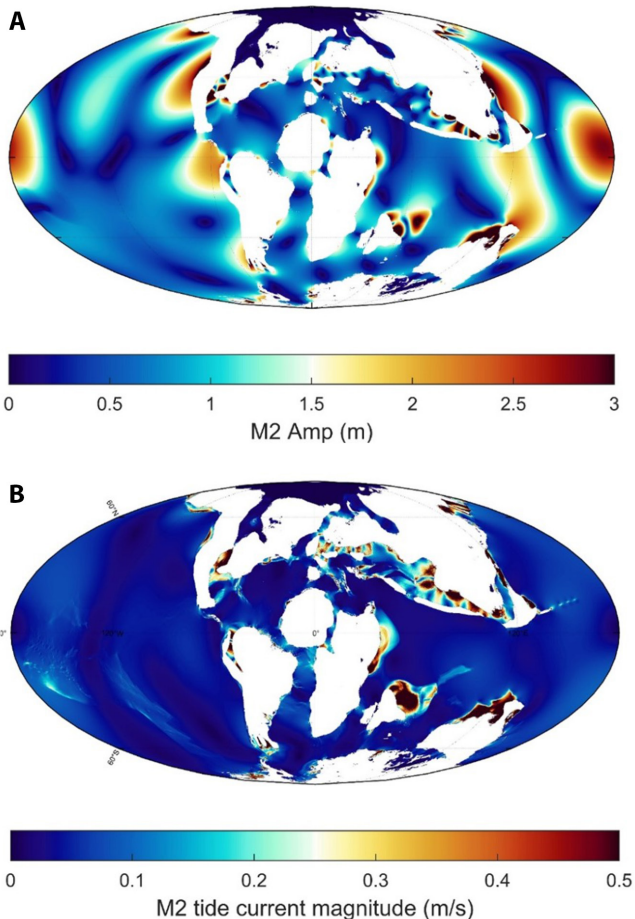

FIGURE 8 (A) Simulated M_2 tidal amplitudes; (B) simulated M_2 tidal current magnitude for the 95 Ma time slice. For clarity, the proxy locations are marked in Figure 9.

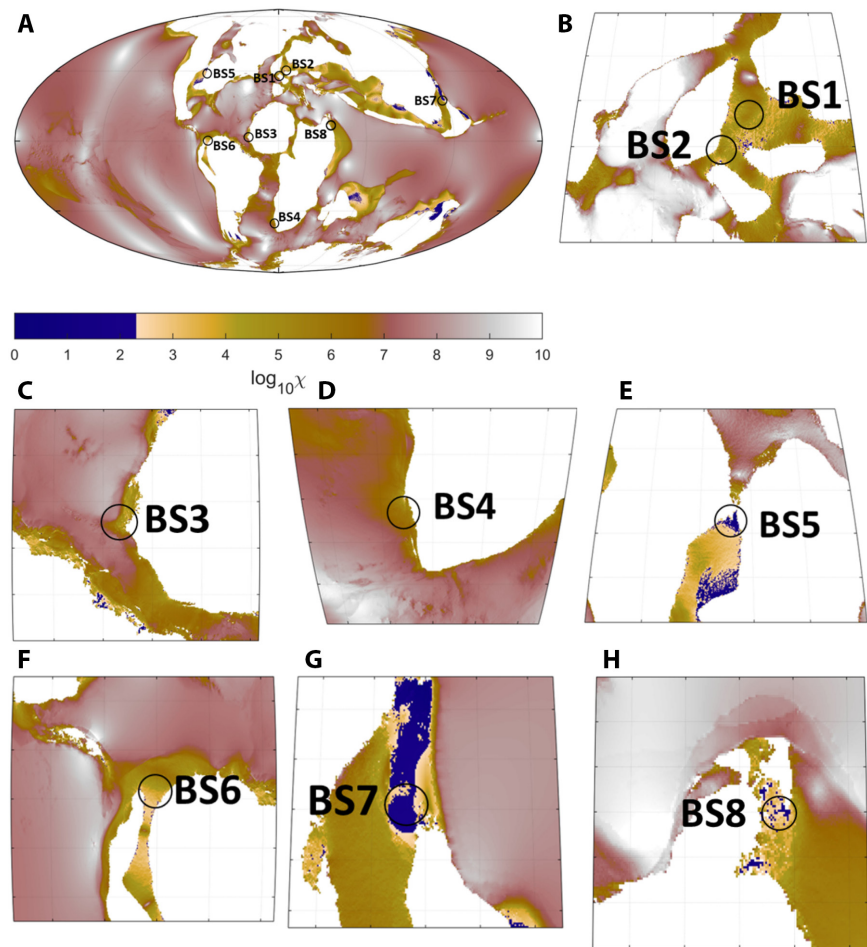FIGURE 9 Predicted Simpson–Hunter criterion for 95 Ma, and the palaeo-location of black shale proxies.

TABLE 3 The model prediction of Simpson–Hunter criterion (logarithms to 10) and the associated tidal stratification for 95 Ma. The locations of black shales are expected to sit in a stratified water column.

	BS6	BS7	BS8	BS9	BS10	BS11	BS12	BS13
$\log_{10}\chi$	3.2	3.6	5.1	6.0	2.0	3.3	1.8	2.5
Water column structure	Stratified	Stratified	Stratified	Stratified	Mixed	Stratified	Mixed	Stratified

the water depth until the model and proxies agree. This way, both verified tidal model simulations and improved reconstructions are obtained.

The main uncertainty in this type of work is in the bathymetric reconstructions because the tidal dynamics are largely controlled by the bathymetry (Byrne et al., 2020; Green et al., 2017, 2020; Zuchuat et al., 2022). The uncertainty or error of the model simulations is given by the RMS value provided; this also highlights that the main uncertainty is the bathymetry. It is very difficult to quantify the uncertainty or accuracy of the proxies, because they are proxies and the modern analogues are largely missing. However, this is largely mitigated by the range of the tidal characteristics from the proxies and if the model simulation falls within that range, there can be confidence in the results for both the model and the proxy. The problem is when the two do not agree and at least one of the

two—the model or the proxy—is incorrect. There is no way of knowing which one at this stage, and more work is needed to improve the model set-up, for example, by using higher resolution in the model simulations and constraining the reconstructions better. This work is underway and left for a future publication.

6 | CONCLUSION

While it can be argued that the results make sense from a dynamical perspective, the encouraging correlations between the model results and proxies show that the model is reasonably correct, and that the methodology works. It also demonstrates that there could be a wealth of viable tidal proxies available in the literature, and that collecting and collating them is a worthy effort to constrain

deep-time tidal model simulations. Two kinds of proxies were explored here, and it is worth investigating further potential proxies found in the literature. For example, grain size distributions could be used alongside bedforms, such as ripples, to provide direct constraints on the current speed (Baas, 1999; Baas et al., 2021; Davis & Dalrymple, 2012; Oost & Baas, 1994). Other proxies can come from palaeobiology, where species distributions can tell us about the size of intertidal zones (and hence tidal range) and, again, help constrain the bathymetry. Matching information of geological formations and basins can also contain estimates of shelf width and specific topography which can be used to further reconstruct bathymetries. The same is true for palaeocurrent directions which could potentially be used to verify shoreline trends. These investigations are left for future publications.

DATA AVAILABILITY STATEMENT
The model bathymetries and associated model outputs, along with Matlab scripts to read the files, are available from 10.5281/zenodo.7684234.

ORCID
B. Guo https://orcid.org/0000-0002-9012-401X
J. M. Hewitt https://orcid.org/0009-0009-7271-505X
J. A. M. Green https://orcid.org/0000-0001-5090-1040

REFERENCES
Abdi, Z., Rimmer, S.M., Rowe, H.D. & Nordeng, S. (2021) Controls on organic matter accumulation in the Bakken Formation, Williston Basin, USA. *Chemical Geology*, 586(October), 120588. https://doi.org/10.1016/j.chemgeo.2021.120588

Aharon, P. (2005) Redox stratification and anoxia of the early Precambrian oceans: implications for carbon isotope excursions and oxidation events. *Precambrian Research*, 137(3–4), 207–222. https://doi.org/10.1016/j.precamres.2005.03.008

Ahokas, J.M., Nystuen, J.P. & Martinius, A.W. (2014) Stratigraphic signatures of punctuated rise in relative sea-level in an estuary-dominated heterolithic succession: incised valley fills of the Toarcian Ostrealv Formation, Neill Klinter Group (Jameson Land, East Greenland). *Marine and Petroleum Geology*, 50, 103–129. https://doi.org/10.1016/j.marpetgeo.2013.11.001

Archer, A.W. (1996) Reliability of lunar orbital periods extracted from ancient cyclic tidal rhythmites. *Earth and Planetary Science Letters*, 141(1–4), 1–10. https://doi.org/10.1016/0012-821X(96)00063-5

Archer, A.W. (2013) World's highest tides: hypertidal coastal systems in North America, South America and Europe. *Sedimentary Geology*, 284, 1–25. https://doi.org/10.1016/j.sedgeo.2012.12.007

Baas, J.H. (1999) An empirical model for the development and equilibrium morphology of current ripples in fine sand. *Sedimentology*, 46(1), 123–138. https://doi.org/10.1046/j.1365-3091.1999.00206.x

Baas, J.H., Malarkey, J., Lichtman, I.D., Amoudry, L.O., Thorne, P.D., Hope, J.A., Peakall, J., Paterson, D.M., Bass, S.J., Cooke, R.D. & Manning, A.J. (2021) Current- and wave-generated bedforms on mixed sand–clay intertidal flats: a new bedform phase diagram and implications for bed roughness and preservation potential. *Frontiers in Earth Science*, 9, 1–27. https://doi.org/10.3389/feart.2021.747567

Balbus, S.A. (2014) Dynamical, biological and anthropic consequences of equal lunar and solar angular radii. *Proceedings of the Royal Society A: Mathematical, Physical and Engineering Sciences*, 470(2168), 20140263. https://doi.org/10.1098/rspa.2014.0263

Bills, B.G. & Ray, R.D. (1999) Lunar orbital evolution: a synthesis of recent results. *Geophysical Research Letters*, 26(19), 3045–3048. https://doi.org/10.1029/1999GL008348

Blackledge, B.W., Green, J.A.M., Barnes, R. & Way, M.J. (2020) Tides on other earths: implications for exoplanet and palaeo-tidal simulations. *Geophysical Research Letters*, 47(12), e2019GL085746. https://doi.org/10.1029/2019GL085746

Bowers, D.G. & Simpson, J.H. (1987) Mean position of tidal fronts in European-shelf seas. *Continental Shelf Research*, 7(1), 35–44. https://doi.org/10.1016/0278-4343(87)90062-8

Byrne, H.M., Green, J.A.M., Balbus, S.A. & Ahlberg, P.E. (2020) Tides: a key environmental driver of osteichthyan evolution and the fish-tetrapod transition? *Proceedings of the Royal Society A: Mathematical Physical and Engineering Sciences*, 476(2242), 20200355. https://doi.org/10.1098/rspa.2020.0355

Collins, D.S., Avdis, A., Wells, M.R., Dean, C.D., Mitchell, A.J., Allison, P.A., Johnson, H.D., Hampson, G.J., Hill, J. & Piggott, M.D. (2021) Prediction of shoreline–shelf depositional process regime guided by palaeotidal modelling. *Earth-Science Reviews*, 223, 103827. https://doi.org/10.1016/j.earscirev.2021.103827

Coughenour, C.L., Archer, A.W. & Lacovara, K.J. (2009) Tides, tidalites, and secular changes in the Earth-Moon system. *Earth-Science Reviews*, 97, 59–79. https://doi.org/10.1016/j.earscirev.2009.09.002

Daher, H., Arbic, B.K., Williams, J.G., Ansong, J.K., Boggs, D.H., Müller, M., Schindelegger, M., Austermann, J., Cornuelle, B.D., Crawford, E.B., Fringer, O.B., Lau, H.C.P., Lock, S.J., Maloof, A.C., Menemenlis, D., Mitrovica, J.X., Green, J.A.M. & Huber, M. (2021) Long-term earth-moon evolution with high-level orbit and ocean tide models. *Journal of Geophysical Research: Planets*, 126(12), e2021JE006875. https://doi.org/10.1029/2021je006875

Dalrymple, R.W., Knight, R.J., Zaitlin, B.A. & Middleton, G.V. (1990) Dynamics and facies model of a macrotidal sand-bar complex, Cobequid Bay—Salmon River Estuary (Bay of Fundy). *Sedimentology*, 37(4), 577–612. https://doi.org/10.1111/j.1365-3091.1990.tb00624.x

Davis, R.A. & Dalrymple, R.W. (Eds.). (2012) *Principles of tidal sedimentology*. New York: Springer. https://doi.org/10.1007/978-94-007-0123-6

Devries Klein, G. (1971) A sedimentary model for determining paleotidal range. *Bulletin of the Geological Society of America*, 82(9), 2585–2592. https://doi.org/10.1130/0016-7606(1971)82[2585:ASMFDP]2.0.CO;2

Egbert, G.D. & Erofeeva, S.Y. (2002) Efficient inverse modeling of barotropic ocean tides. *Journal of Atmospheric and Oceanic Technology*, 19(2), 183–204. https://doi.org/10.1175/1520-0426(2002)019<0183:EIMOBO>2.0.CO;2

Egbert, G.D., Ray, R.D. & Bills, B.G. (2004) Numerical modeling of the global semidiurnal tide in the present day and in the last glacial maximum. *Journal of Geophysical Research: Oceans*, 109(C3), 1–15. https://doi.org/10.1029/2003JC001973

Green, J.A.M., Davies, H.S., Duarte, J.C., Creveling, J.R. & Scotese, C. (2020) Weak tides during Cryogenian glaciations. *Nature Communications*, 11(1), 6227. https://doi.org/10.1038/s41467-020-20008-3

Green, J.A.M., Hadley-Pryce, D. & Scotese, C.R. (2022) Phanerozoic (541 Ma to present day). In: Green, J.A.M. & Duarte, J.C. (Eds.), *A journey through tides*. Amsterdam, Netherlands: Elsevier, p. 600.

Green, J.A.M., Huber, M., Waltham, D., Buzan, J. & Wells, M. (2017) Explicitly modelled deep-time tidal dissipation and its implication for Lunar history. *Earth and Planetary Science Letters*, 461, 46–53. https://doi.org/10.1016/j.epsl.2016.12.038

Green, J.A.M., Molloy, J.L., Davies, H.S. & Duarte, J.C. (2018) Is there a tectonically driven supertidal cycle? *Geophysical Research Letters*, 45(8), 3568–3576. https://doi.org/10.1002/2017GL076695

Green, J.A.M. & Nycander, J. (2013) A comparison of tidal conversion parameterizations for tidal models. *Journal of Physical Oceanography*, 43(1), 104–119. https://doi.org/10.1175/JPO-D-12-023.1

Griffing, D.H., Bridge, J.S. & Hotton, C.L. (2000) Coastal-fluvial palaeoenvironments and plant palaeoecology of the Lower Devonian (Emsian), Gaspé Bay, Québec, Canada. *Geological Society, London, Special Publications*, 180(1), 61–84. https://doi.org/10.1144/GSL.SP.2000.180.01.05

He, T., Wignall, P.B., Newton, R.J., Atkinson, J.W., Keeling, J.F.J., Xiong, Y. & Poulton, S.W. (2022) Extensive marine anoxia in the European epicontinental sea during the end-Triassic mass extinction. *Global and Planetary Change*, 210(February), 103771. https://doi.org/10.1016/j.gloplacha.2022.103771

Kadiri, M., Zhang, H., Angeloudis, A. & Piggott, M.D. (2021) Evaluating the eutrophication risk of an artificial tidal lagoon. *Ocean and Coastal Management*, 203, 105490. https://doi.org/10.1016/j.ocecoaman.2020.105490

Kassem, A.A., Sharaf, L.M., Baghdady, A.R. & El-Naby, A.A. (2020) Cenomanian/Turonian oceanic anoxic event 2 in October oil field, central Gulf of Suez, Egypt. *Journal of African Earth Sciences*, 165, 103817. https://doi.org/10.1016/j.jafrearsci.2020.103817

Kimura, H. & Watanabe, Y. (2001) Oceanic anoxia at the Precambrian-Cambrian boundary. *Geology*, 29(11), 995–998. doi:10.1130/0091-7613(2001)029<0995:OAATPC>2.0.CO;2

Klatt, J.M., Chennu, A., Arbic, B.K., Biddanda, B.A. & Dick, G.J. (2021) Possible link between Earth's rotation rate and oxygenation. *Nature Geoscience*, 14, 564–570. https://doi.org/10.1038/s41561-021-00784-3

Klein, G.D. (1970) Depositional and dispersal dynamics of intertidal sand bars. *Journal of Sedimentary Research*, 40(4), 1095–1127. doi:10.1306/74D72144-2B21-11D7-8648000102C1865D

Klein, G.D. (1971) A sedimentary model for determining paleotidal range. *Bulletin of the Geological Society of America*, 82(9), 2585–2592. doi:10.1130/0016-7606(1971)82[2585:ASMFDP]2.0.CO;2

McArthur, J.M., Algeo, T.J., van de Schootbrugge, B., Li, Q. & Howarth, R.J. (2008) Basinal restriction, black shales, Re-Os dating, and the Early Toarcian (Jurassic) oceanic anoxic event. *Paleoceanography*, 23(4). https://doi.org/10.1029/2008PA001607

Monteiro, F.M., Pancost, R.D., Ridgwell, A. & Donnadieu, Y. (2012) Nutrients as the dominant control on the spread of anoxia and euxinia across the Cenomanian-Turonian oceanic anoxic event (OAE2): model-data comparison. *Paleoceanography*, 27(4). https://doi.org/10.1029/2012PA002351

Nielsen, H.L., Larsen, F. & Frandsen, N. (1989) Upper Triassic-Lower Jurassic tidal deposits of the Gassum Formation on Sjælland, Denmark. *Danmarks Geologiske Undersøgelse Serie A*, 23, 1–30. https://doi.org/10.34194/seriea.v23.7043

Oost, A.P. & Baas, J.H. (1994) The development of small scale bedforms in tidal environments: an empirical model for unsteady flow and its applications. *Sedimentology*, 41(5), 883–903. https://doi.org/10.1111/j.1365-3091.1994.tb01430.x

Price, D., Stuiver, C., Johnson, H., Gallego, A. & O'Hara Murray, R. (2016) The Scottish Shelf Model. Part 4: East coast of Lewis and Harris sub-domain. *Scottish Marine and Freshwater Science*, 7(6), 147.

Pugh, D.T. (1987) *Tides, surges and mean sea level*. John Wiley & Sons.

Qiu, Z. & He, J. (2022) Depositional environment changes and organic matter accumulation of Pliensbachian-Toarcian lacustrine shales in the Sichuan Basin, SW China. *Journal of Asian Earth Sciences*, 232, 105035. https://doi.org/10.1016/j.jseaes.2021.105035

Reineck, H.E. (1975) German North Sea tidal flats. In: Ginsburg, R.N. (Ed.) *Tidal deposits*. Berlin, Heidelberg: Springer. https://doi.org/10.1007/978-3-642-88494-8_1

Rust, B.R., Lawrence, D.A. & Zaitlin, B.A. (1989) The sedimentology and tectonic significance of Devonian and Carboniferous terrestrial successions in Gaspe, Quebec. *Atlantic Geology*, 25(1), 1–13. https://doi.org/10.4138/1666

Scotese, C.R. & Wright, N. (2018) PALEOMAP Paleodigital Elevation Models (PaleoDEMS) for the Phanerozoic PALEOMAP Project. https://www.earthbyte.org/paleodem-resourcescotese-and-wright-2018/

Scourse, J.D., Austin, W.E.N., Long, B.T., Assinder, D.J. & Huws, D. (2002) Holocene evolution of seasonal stratification in the Celtic Sea: refined age model, mixing depths and foraminiferal stratigraphy. *Marine Geology*, 191(3–4), 119–145. https://doi.org/10.1016/S0025-3227(02)00528-5

Sellwood, B.W. (1972) Tidal-flat sedimentation in the Lower Jurassic of Bornholm, Denmark. *Palaeogeography, Palaeoclimatology, Palaeoecology*, 11(2), 93–106. https://doi.org/10.1016/0031-0182(72)90012-0

Sharples, J., Tweddle, J.F., Green, J.A.M., Palmer, M.R., Kim, Y.-N., Hickman, A.E., Holligan, P.M., Moore, C.M., Rippeth, T.P., Simpson, J.H. & Krivtsov, V. (2007) Spring-neap modulation of internal tide mixing and vertical nitrate fluxes at a shelf edge in summer. *Limnology and Oceanography*, 52(5), 1735–1747. https://doi.org/10.4319/lo.2007.52.5.1735

Simpson, J.H. & Bowers, D. (1981) Models of stratification and frontal movement in shelf seas. *Deep Sea Research Part A:*

Oceanographic Research Papers, 28(7), 727–738. https://doi.org/10.1016/0198-0149(81)90132-1

Simpson, J.H. & Hunter, J.R. (1974) Fronts in the Irish Sea. *Nature*, 250(2), 404–406. https://doi.org/10.1038/250404a0

Slingerland, R. (1986) Numerical computation of co-oscillating palaeotides in the Catskill epeiric Sea of eastern North America. *Sedimentology*, 33(4), 487–497. https://doi.org/10.1111/j.1365-3091.1986.tb00756.x

Stammer, D., Ray, R.D., Andersen, O.B., Arbic, B.K., Bosch, W., Carrère, L., Cheng, Y., Chinn, D.S., Dushaw, B.D., Egbert, G.D., Erofeeva, S.Y., Fok, H.S., Green, J.A.M., Griffiths, S., King, M.A., Lapin, V., Lemoine, F.G., Luthcke, S.B., Lyard, F., Morison, J., Müller, M., Padman, L., Richman, J.G., Shriver, J.F., Shum, C.K., Taguchi, E. & Yi, Y. (2014) Accuracy assessment of global barotropic ocean tide models. *Reviews of Geophysics*, 52(3), 243–282. https://doi.org/10.1002/2014RG000450

Stow, D.A.V., Huc, A.-Y. & Bertrand, P. (2001) Depositional processes of black shales in deep water. *Marine and Petroleum Geology*, 18, 491–498. https://doi.org/10.1016/S0264-8172(01)00012-5

Takashima, R., Nishi, H., Yamanaka, T., Hayashi, K., Waseda, A., Obuse, A., Tomosugi, T., Deguchi, N. & Mochizuki, S. (2010) High-resolution terrestrial carbon isotope and planktic foraminiferal records of the Upper Cenomanian to the Lower Campanian in the Northwest Pacific. *Earth and Planetary Science Letters*, 289(3–4), 570–582. https://doi.org/10.1016/j.epsl.2009.11.058

Tanavsuu-Milkeviciene, K. & Plink-Bjorklund, P. (2009) Recognizing tide-dominated versus tide-influenced deltas: middle Devonian strata of the Baltic Basin. *Journal of Sedimentary Research*, 79(12), 887–905. https://doi.org/10.2110/jsr.2009.096

Taylor, G.I. (1920) Tidal friction in the Irish Sea. *Proceedings of the Royal Society of London Series A*, 96, 1–33. https://doi.org/10.1098/rsta.1920.0001

Tessier, B. (2023) Tidal rhythmites: their contribution to the characterization of tidal dynamics and environments. In: Green, M. & Duarte, J.C. (Eds.), *A journey through tides*. Amsterdam, the Netherlands: Elsevier, pp. 283–305. https://doi.org/10.1016/B978-0-323-90851-1.00015-7

Tessier, B. & Gigot, P. (1989) A vertical record of different tidal cyclicities: an example from the Miocene Marine Molasse of Digne (Haute Provence, France). *Sedimentology*, 36(5), 767–776. https://doi.org/10.1111/j.1365-3091.1989.tb01745.x

Tovmasjana, K. (2013) *Depositional environment of the tidally-dominated transgressive succession: Rezekne and Pärnu regional stages, Baltic Devonian Basin*. Latvia: University of Latvia.

Tuerena, R.E., Williams, R.G., Mahaffey, C., Vic, C., Green, J.A.M., Naveira-Garabato, A., Forryan, A. & Sharples, J. (2019) Internal tides drive nutrient fluxes into the deep chlorophyll maximum over mid-ocean ridges. *Global Biogeochemical Cycles*, 33(8), 995–1009. https://doi.org/10.1029/2019GB006214

Ward, S.L., Scourse, J.D., Yokoyama, Y. & Neill, S.P. (2020) The challenges of constraining shelf sea tidal models using seabed sediment grain size as a proxy for tidal currents. *Continental Shelf Research*, 205, 104165. https://doi.org/10.1016/j.csr.2020.104165

Wells, M.R., Allison, P.A., Hampson, G.J., Piggott, M.D. & Pain, C.C. (2005) Modelling ancient tides: the Upper Carboniferous epi-continental seaway of Northwest Europe. *Sedimentology*, 52(4), 715–735. https://doi.org/10.1111/j.1365-3091.2005.00718.x

Wells, M.R., Allison, P.A., Piggott, M.D., Hampson, G.J., Pain, C.C. & Gorman, G.J. (2010) Tidal modeling of an ancient tide-dominated seaway, part 1: model validation and application to global early cretaceous (aptian) tides. *Journal of Sedimentary Research*, 80(5–6), 393–410. https://doi.org/10.2110/jsr.2010.044

Wendt, J., Kaufmann, B., Belka, Z., Farsan, N. & Karimi Bavandpur, A. (2004) Devonian/Lower Carboniferous stratigraphy, facies patterns and palaeogeography of Iran Part II. Northern and central Iran. *Acta Geologica Polonica*, 55(1), 31–97.

Wignall, P.B. & Newton, R. (2001) Black shales on the basin margin: a model based on examples from the Upper Jurassic of the Boulonnais, northern France. *Sedimentary Geology*, 144(3–4), 335–356. https://doi.org/10.1016/S0037-0738(01)00125-7

Williams, G.E. (2000) Geological constraints on the Precambrian history of Earth's rotation and the Moon's orbit. *Reviews of Geophysics*, 38, 37–59. https://doi.org/10.1029/1999RG900016

Wilmes, S.-B. & Green, J.A.M. (2014) The evolution of tides and tidal dissipation over the past 21,000 years. *Journal of Geophysical Research: Oceans*, 119(7), 4083–4100. https://doi.org/10.1002/2013JC009605

Wilmes, S.-B., Green, J.A.M. & Schmittner, A. (2021) Was vertical mixing in the glacial ocean enhanced? *Nature Communications Earth and Environment*, 2(166), 1–9. https://doi.org/10.1038/s43247-021-00239-y

Wunsch, C. & Ferrari, R. (2004) Vertical mixing, energy, and the general circulation of the oceans. *Annual Review of Fluid Mechanics*, 36(1), 281–314. https://doi.org/10.1146/annurev.fluid.36.050802.122121

Zand-Moghadam, H., Moussavi-Harami, R. & Mahboubi, A. (2014) Sequence stratigraphy of the Early-Middle Devonian succession (Padeha Formation) in Tabas Block, East-Central Iran: implication for mixed tidal flat deposits. *Palaeoworld*, 23(1), 31–49. https://doi.org/10.1016/j.palwor.2013.06.002

Zaron, E.D. & Egbert, G.D. (2006) Estimating open-ocean barotropic tidal dissipation: the Hawaiian Ridge. *Journal of Physical Oceanography*, 36(6), 1019–1035. https://doi.org/10.1175/JPO2878.1

Zuchuat, V., Steel, E., Mulligan, R.P., Collins, D.S. & Green, J.A.M. (2022) Tidal dynamics in palaeo-seas in response to changes in physiography, tidal forcing and bed shear stress. *Sedimentology*, 69(4), 1861–1890. https://doi.org/10.1111/sed.12975

SUPPORTING INFORMATION

Additional supporting information can be found online in the Supporting Information section at the end of this article.